Materials Chemistry and Physics 200 (2017) 342–353

Contents lists available at ScienceDirect

Materials Chemistry and Physics

journal homepage: www.elsevier.com/locate/matchemphys

Precipitation kinetics in a 10.5%Cr heat resistant steel: Experimental results and simulation by TC-PRISMA/DICTRA

J.P. Sanhueza [a, **], D. Rojas [a, *], O. Prat [a], J. Garcia [b], R. Espinoza [c], C. Montalba [d], M.F. Melendrez [a]

[a] Universidad de Concepción, Departamento de Ingeniería de Materiales, Edmundo Larenas 270, Concepción, Chile
[b] AB SandvikCoromant R&D, Lerkrogsvägen 19, Stockholm, SE 126 80, Sweden
[c] Universidad de Chile, Departamento de Ciencia de Los Materiales, Av. Tupper, 2069, Santiago, Chile
[d] Universidad de Talca, Departamento de Tecnologías Industriales, Camino a Los Niches KM 1, Curicó, Chile

HIGHLIGHTS

- Design, production and characterization of 10%Cr steel assisted by ThermoCalc.
- Long term aging (8760 h) and TEM characterization of $M_{23}C_6$, MX and Laves phase.
- Simulation of nucleation-growth-coarsening of $M_{23}C_6$ and Laves by PRISMA and DICTRA.
- The effect of Boron on $M_{23}C_6$ carbides was satisfactory simulated by PRISMA.
- PRISMA simulation of Laves Phase considering micrograin segregation of Si and W.

GRAPHICAL ABSTRACT

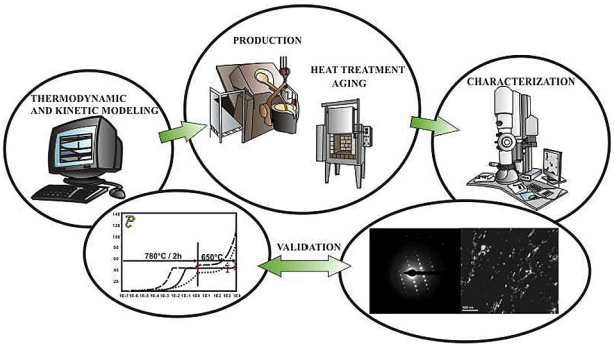

ARTICLE INFO

Article history:
Received 12 January 2017
Received in revised form
14 June 2017
Accepted 29 July 2017
Available online 7 August 2017

Keywords:
TC-PRISMA
DICTRA
Modeling
Heat resistant steels
TEM characterization

ABSTRACT

The precipitation kinetics of secondary phases in a 10.5%Cr heat resistant steel, designed by the authors, was studied experimentally and theoretically. Experimental data of nucleation, growth and coarsening stages for $M_{23}C_6$ carbides, V-MX, Nb-MX and Laves phase were obtained by HRTEM-characterization on samples after tempering (780°C/2 h) and isothermally aging for 1440 h and 8760 h at 650 °C. Theoretical studies of precipitation behavior of $M_{23}C_6$ and Laves phase were carried out by TC-PRISMA and complemented with DICTRA. A good fit between TC-PRISMA simulation and experimental results was obtained for $M_{23}C_6$ carbides considering a heterogeneous nucleation in grain boundaries, a semi-coherent interfacial energy of 0.3 J/m^2, and decreasing the atomic mobility along grain boundary in order to include the effect of B. Experiments and simulation indicate a low coarsening rate for $M_{23}C_6$ carbides. Furthermore, precipitation of Laves phase at 650 °C was simulated by TC-PRISMA considering the effect of W and Si segregation at grain boundary, prior to the beginning of the nucleation and growth processes. Therefore, thermodynamic and kinetic boundary conditions were changed purposely in TC-PRISMA. Best agreement with the experimental results was obtained for an interfacial energy of 0.6 J/m^2 and heterogeneous nucleation in grain boundary.

* Corresponding author.
** Corresponding author.
E-mail address: davrojas@udec.cl (D. Rojas).

http://dx.doi.org/10.1016/j.matchemphys.2017.07.083
0254-0584/

1. Introduction

The reduction of carbon dioxide emissions in the energy industry is a relevant research field due to new environmental regulations and worldwide demand for clean energy [1]. Nowadays fossil-fire power plants produce about 42% of global electric energy and it is expected to continue as the main energy production source during the next 30 years [2]. Reduction of carbon dioxide emissions is strongly related to the thermal efficiency of the process, which is mainly controlled by the service temperature and pressure of power plants. Indeed, rising the service temperature and pressure from 540°C/18 MPa to 600°C/30 MPa has led to a thermal efficiency increase of about 10%, and a reduction in the specific carbon dioxide emissions of about 30% [3]. Martensitic/Ferritic 9–12%Cr heat resistant steels (all values referred in this work are in wt%) are key materials for further improving the thermal efficiency in power plants. They offer the best combination of high creep strength, low thermal expansion coefficient, high resistance against thermal fatigue, high steam oxidation resistance, low cost and good manufacturability, operating in the creep range at temperatures of up to 600 °C [4]. Their good properties at high temperatures are related to their unique microstructure, which contains high dislocation density and several different internal interfaces, such as: prior austenite grain boundaries (PAGB), block boundaries, prior martensite lath boundaries and sub-grain boundaries [5]. In addition, high creep resistance is given by the combination of different precipitates uniformly distributed through the microstructure, e.g. $M_{23}C_6$ carbides, MX carbonitrides and Laves phase. These particles stabilize free dislocations and sub-grain boundaries delaying the microstructure recovery [6,7]. Nevertheless, the increase of working temperature (up to 650 °C) and exposure to stress during service promotes microstructural degradation, coarsening of precipitates (e.g. Laves, $M_{23}C_6$) and precipitation of undesirable phases (e.g. Z-phase), which is reflected in a decrease in creep strength [8–10]. The coarsening of precipitates follows the Ostwald ripening mechanism [3], where average precipitate volume increases with time at elevated temperatures. As a result, spacing of the precipitates increases and particle hardening diminishes [11]. The stability of precipitates distributed through the microstructure contributes to avoid the recovery of the microstructure, pinning the movement of dislocations and sub-grain boundaries enhancing the creep strength [12,13]. Therefore, the experimental study of the particles at 650 °C, correlated by new modeling techniques which simulate stability and evolution of the phases during service, is fundamental to understand the effect of microstructure on creep strength.

In previous studies, the authors designed and produced four 9% Cr heat resistant steels for creep conditions at 650 °C and 100 MPa [10]. The microstructure evolution of these 9%Cr steels was investigated during creep at 100MPa/650°C/13000 h focusing on quantitative later further study, the experimental STEM quantification of 9%Cr heat resistant steel (designed and produced by the authors) was compared with TC-PRISMA software calculations, related to the nucleation and growth of precipitates, and DICTRA computational modeling for coarsening. The simulations performed by both programs were focused on the nucleation, growth and coarsening of $M_{23}C_6$carbides, Nb-MX and V-MX carbonitrides at long-term creep conditions [14]. The main objective of the present study was to design and produce a 10.5%Cr heat resistant steel supported by Thermo-Calc. In addition, the study aims to characterize the precipitates in the initial state, after 1440 h and 8640 h at 650 °C, to compare the observed evolution of the microstructure regarding the kinetic of precipitation of $M_{23}C_6$ carbides and Laves phase, with the calculations carried out by TC-PRISMA and DICTRA.

2. Experimental procedure

2.1. Thermodynamic modeling

Thermo-Calc software package based on the CALPHAD method has been successfully employed for alloy design considering multicomponent and multiphase systems [5,15]. At the heart of this method is the calculation of the Gibbs energy of a phase as a function of its composition temperature and pressure. Within this approach, the problem of predicting equilibrium and evaluation of phase stability is essentially mathematical, although far from simple due to the number of variables involved in the minimization process [16]. The software is linked with various databases and interfaces, where all the thermodynamic information as Gibbs energy is stored. Upon modeling, time and costs of trial-and-error of conventional alloy development can be reduced [10,15]. All calculations were carried out with the Thermo-Calc database TCFe7 [17].

2.2. TC-PRISMA modeling (Nucleation, growth and coarsening)

TC-PRISMA software simulates nucleation, growth and coarsening of precipitates in multicomponent and multiphase systems by the Larger-Schwartz approach [18]. To simulate nucleation, this method considers the clusters as embryos of new phases with different structure or compositions. The time dependent nucleation rate $J(t)$ is defined as:

$$J(t) = J_s \exp\left(-\frac{\tau}{t}\right) \tag{1}$$

J_s denotes the steady state nucleation rate, τ means the incubation time for establishing steady state nucleation conditions, and t is the isothermal reaction time. The incubation time for an isothermal reaction can be expressed by:

$$\tau = \frac{1}{\theta Z^2 \beta^*} \tag{2}$$

whereθdiffers from one derivation to another. According to Feder et al. [19]θnormally adopts the value 2. The expression Z and β^*will be explained in the following. The steady state nucleation rate Js can be written as:

$$J_s = Z\beta^* N_0 \exp\left(-\frac{\Delta G^*}{kT}\right) \tag{3}$$

Z denotes the Zeldovichfactor, $\beta^*$is the rate at which atoms or molecules are attached to the critical nucleus, $N_0$is the number of available nucleation sites per unit volume. ΔG^*refers to the Gibbs energy of formation of a critical nucleus, $k$is Boltzmann's constant, and T means the absolute temperature.

The Gibbs formation energy of a critical nucleus can be written as:

$$\Delta G^* = \frac{16\pi\sigma^3}{3\left(\Delta G_m^{\alpha\to\beta} / V_m^{\beta}\right)^2} \tag{4}$$

σrefers to the interfacial energy, $\Delta G_m^{\alpha\to\beta}$is the molar Gibbs energy change for the formation of the β particles with critical composition $X_i^{\beta}$from the αmatrix. This means the maximum driving force for the $\alpha\to\beta$ phase transformation. The maximum driving force and the critical composition can be obtained by the Newton-Raphson method [20], which is a calculation routine in the Thermo-Calc

software.

Nucleation can be considered as a diffusion process in the particle size space. Supercritical nuclei with radius slightly larger than the critical radius have a probability of passing back across the free energy barrier and dissolve in the matrix. The measure of such probability is the Zeldovich factor Z and depends upon the thermodynamics of the nucleation process. The critical radius r^* is given by:

$$r^* = -\frac{2\sigma V_m^{\beta}}{\Delta G_m^{\alpha\rightarrow\beta}} \tag{5}$$

The atomic or molecular attachment rate β^* reflects the kinetics of mass transport in the nucleation process and is given by Ref. [21]:

$$\beta^* = \frac{4\pi r^{*2}}{a^4}\left[\sum_{i=1}^{k}\frac{\left(X_i^{\beta/\alpha}-X_i^{\alpha/\beta}\right)^2}{X_i^{\alpha/\beta}D_i}\right]^{-1} \tag{6}$$

a denotes the lattice parameters, $X_i^{\beta/\alpha}$ and $X_i^{\alpha/\beta}$ are the mole fractions of element i at the interface in the precipitate and matrix, respectively. D_i is the corresponding diffusion coefficient in the matrix.

2.3. DICTRA modeling (coarsening theory)

DICTRA is a software for simulation of diffusion controlled transformations in multicomponent systems based on numerical solution of the diffusion equations in systems [22]. The accuracy of the simulations is strongly dependent on the thermodynamic and kinetic database used, but also on the border conditions, such as choice of geometry [23]. DICTRA software adopts the Ostwald ripening model to simulate coarsening. Coarsening is the late stage of precipitation kinetics when larger precipitates grow on the expense of smaller precipitates which dissolve [24]. The coarsening model in DICTRA uses the fact that the additional pressure caused by the curved interface induces a shift in the local equilibrium at the interface between a precipitate phase and a matrix phase and, consequently, displaces the concentrations. It uses the approximation that the coarsening of a system could be described by performing calculations on one single spherical particle (β) embedded in a spherical matrix phase (α) [25]. Additionally, DICTRA considers that particle size distribution follows the Lifshitz-Slyozov-Wagner distribution. The composition of the particles present in the alloy was calculated by Thermo-Calc with database TCFe7 [17]. The coarsening simulations were carried out by the mobility database MOBFe2 [26]. The relationship between the volume fraction of precipitates and the radius of particles was calculated by the following expression:

$$V_f^{Particle} = \frac{V_1}{V_2} = \frac{R_1^3}{R_2^3} \tag{7}$$

where $V_f^{Particle}$ is the volume fraction of particles ($M_{23}C_6$, Nb-MX or V-MX), V_1 is the volume of particle and V_2 is the volume of the cell. R_1 and R_2 are the radius of particle and the cell radius respectively. Cell size was calculated by:

$$R_2 = \sqrt[3]{\frac{R_1^3}{V_f^{Particle}}} \tag{8}$$

2.4. Alloy production

The alloy was prepared by vacuum induction melting with masses of about 9 kg. The final chemical composition of the alloys is shown in Table 1.

Samples were hot-rolled, austenitized and tempered with the following parameters:

- Hot-rolling at 1100 °C with posterior air cooling (60% final deformation).
- Austenitization heat treatment at 1080 °C by 0.5 h followed by air-cooling.
- Tempering heat treatment at 780 °C by 2 h with subsequent air-cooling

The heat treatment temperatures are indicated in Fig. 1. Measurement of the chemical composition was carried out by optical emission spectroscope (SpectroMaxx).

2.5. Microstructure investigation

The alloy microstructure was analyzed in the initial state (tempering 780°C/2 h), after 1440 h and 8760 h at 650 °C by STEM (Hitachi S5500 operating at 300 kV, maximum resolution of 0.4 nm) and HRTEM (JEOL JEM-ARM200F operating at 200 kV, maximum resolution of 0.08 nm). Samples were prepared by the carbon extracted replication method. Carbon extracted replicas provide more accurate measurements of the chemical composition and crystallographic structure of the precipitates [27]. The carbon extracted replicas were prepared by Vilella's etching. Observations were carried out in the bright field (BF) and scanning mode (STEM). Precipitates were identified by a combination of electron diffraction patterns (DP) and energy dispersive spectroscopy (EDS) analysis and line scan analysis, to avoid ambiguous identification of similar precipitates. Equivalent circle diameters of the particles were calculated with an image editor in order to carry out a quantitative analysis of precipitates [28]. More than 100 particles for $M_{23}C_6$ carbides, Laves phase, Nb-MX and V-MX were quantified to ensure reliability of the measurements. In the case that the particles presented a non-spherical form, two perpendicular axes were measured (a and b) and an average diameter (a+b)/2 was calculated. Several micrographs from the sample section were analyzed in order to ensure that measurements were representative for the whole material.

2.6. Annealing tests

Isothermal aging was carried out in air at 650 °C (±5 K) for 1440 h and 8760 h. Samples of about one cubic centimeter were used to perform the isothermal aging.

2.7. Hardness

Vickers hardness measurements (HV_{10}) according to DIN EN ISO 6507-1 were carried out. At least 10 measurements were performed on the samples in the initial and after isothermal aging to ensure measurements were representative.

Table 1
Analyzed chemical composition of the produced alloy (wt%).

C	Si	Mn	Co	B	Cr	W	V	N	Nb	Fe
0.11	0.40	0.42	0.95	0.01	10.5	2.0	0.16	0.01	0.03	Bal.

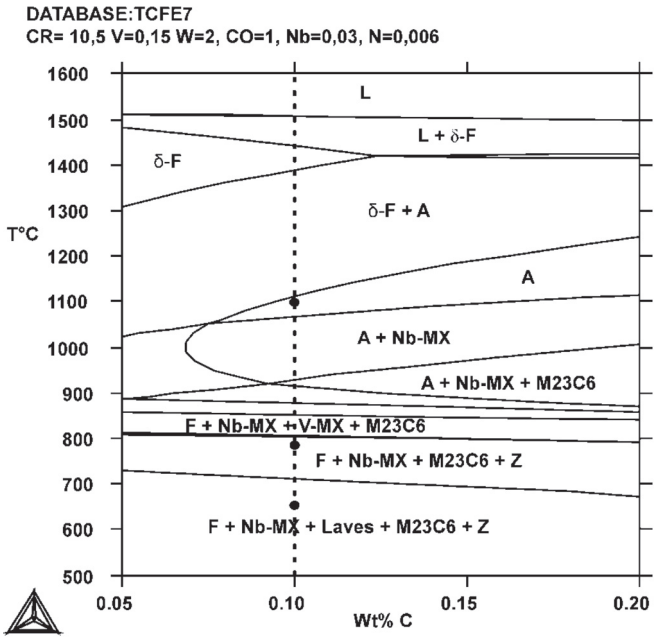

Fig. 1. Thermo-Calc phase diagram alloy 10.5CrWVNb (F = ferrite, A = austenite). The austenitization, tempering and ageing temperatures are indicated in the phase diagram by black circles. V-MX indicates V-rich, Nb-MX denotes Nb-rich particles.

3. Results and discussion

3.1. Alloy design

The alloy 10.5CrVNb was designed considering basic metallurgical principles and thermodynamic calculations (Thermo-Calc) in order to obtain a tailor made microstructure and to reduce the time and costs of trial-and-error of conventional alloy development [10]. The alloy was designed to obtain a Martensitic/Ferritic matrix, $M_{23}C_6$ carbides, Nb and V rich carbonitrides and Laves phase at the service temperature (650 °C, see Fig. 1).

10.5%Cr was added in order to improve the corrosion and oxidation resistance at high temperature without drastically decreasing creep strength. It has been demonstrated that high Cr content increases the driving force for the precipitation of Z-phase [29,30]. The decrease of creep strength is related to the transformation of V-MX and Nb-MX particles into Z-phase by Cr diffusion from the matrix. The V-MX and Nb-MX carbonitrides are considered to provide an important contribution to creep resistance, because they block the dislocations and sub-grain boundaries increasing the creep strength [13].

2% of W was set in order to stabilize Laves phase at 650 °C (see Fig. 1). It has been reported that Laves phase provides a pinning force that reduces the migration of block and martensite lath boundaries retarding the microstructural degradation [8]. Nevertheless, larger amounts of W promote the formation of delta ferrite during solidification [31].

The Co content was set at 1% to avoid the formation of delta ferrite during solidification and stabilize the austenitic field [32]. Additionally, Co may slow down the diffusion of atoms in metals, because diffusion depends on ferromagnetic state. The ferromagnetic state of the steel is altered with the addition of Co since this element may raise the curie temperature of the steel [4,5,33]. Furthermore Co increases the driving force of Laves phase precipitation, since Co decreases the solubility of W in the matrix [9].

B content was set at 0.01% in order to stabilize the $M_{23}C_6$ carbides by reducing the Ostwald ripening rate in the vicinity of prior austenite boundaries [34,35]. The relation ratio between B and N was carefully balanced in order to avoid the formation of BN particles that considerably reduce the creep strength [34].

About 0.01% of N was added together with 0.16% of V and 0.03% Nb to promote the formation of Nb-MX and V-MX carbonitrides. V and Nb in combination with C and N form stable carbides and carbonitrides, which provide the necessary precipitation strengthening due to the low coarsening rate of such precipitates [36].

3.2. Thermodynamic modeling results

According to the phase diagram calculated by Thermo-Calc, the austenitization temperature was chosen at 1080 °C. This temperature ensures a fully austenitic field and promotes the dissolution of most particles formed during solidification. A fully martensitic transformation is expected and the formation of delta ferrite is avoided during heat treatment.

The heat treatment temperature (780 °C) was chosen to temper the martensitic matrix obtained after the austenitization and subsequent air cooling. During tempering the hard and brittle martensite is softened and nucleation and growth of $M_{23}C_6$, Nb-MX and V-MX particles are expected [14]. The equilibrium volume fractions of all present phases at 780 °C are shown in Table 2. The V-MX particles are not thermodynamically stable at the tempering temperature due to the high Cr content of this alloy. According to the phase diagram, Z-phase particles presented higher stability in comparison to V-MX particles at 650 °C. Cipolla et al. [29] demonstrated that the progress of the Z-phase is associated to the consumption of small finely dispersed V-MX particles by uptake of Cr from the matrix. Therefore, V-MX precipitates are gradually transformed into Z-phase. Despite the calculations, no Z-phase particles are expected in the initial state after tempering. At the service temperature (650 °C), the stables phases are Ferrite, $M_{23}C_6$ carbides, Nb-MX carbonitrides, Laves Phase and Z-phase (see Table 2). The nucleation and growth of Laves phase occur at the service conditions and no Laves phase is expected after tempering.

3.3. Microstructural characterization

The alloy microstructure at the initial state and after the isothermal aging condition showed a martensite/ferrite matrix with high density of interfaces such as: prior austenite grain boundaries, block and martensite lath, sub-grain boundaries and precipitates. Furthermore, the martensitic transformation provides high dislocation density even after tempering at 780 °C [37]. STEM and HRTEM studies were carried out to quantify the microstructure features in the initial state and after isothermal aging at 650 °C.

3.3.1. Initial microstructure

The STEM image (Fig. 2) was obtained from a carbon extracted replica, the image shows two types of boundaries: PAGB and lath or block boundaries. The identification of these two types of

Table 2
Volume fraction of precipitates calculated by Thermo-Calc at 780 °C and 650 °C.

Phase	Volume Fraction	
	780 °C	650 °C
Ferrite	98.00	97.26
$M_{23}C_6$	1.93	1.96
Nb-MX	0.02	0.02
Laves	–	0.61
Z (V-MX)	0.05	0.07

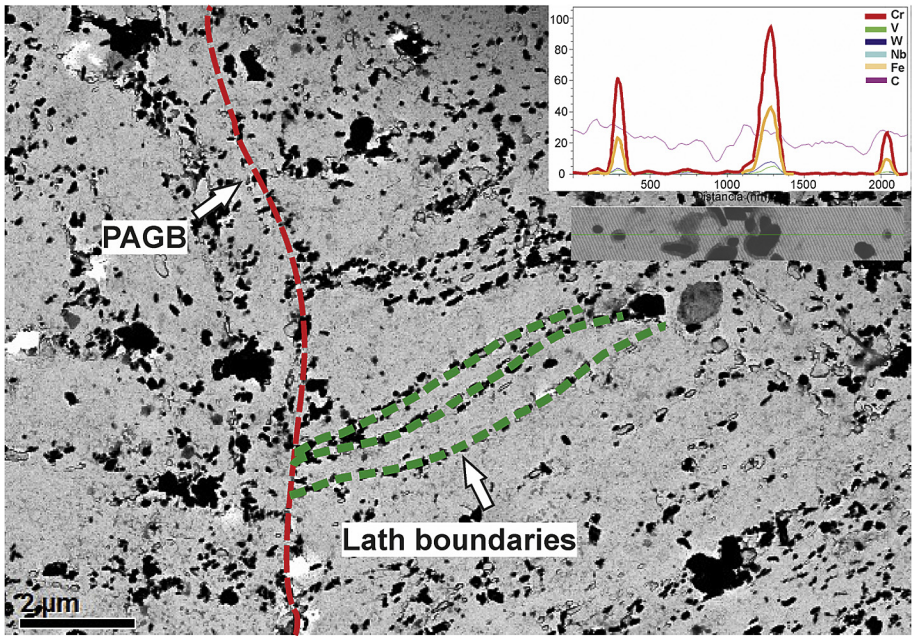

Fig. 2. STEM image, carbon extracted replication of the alloy 10.5CrWVNb (bright field) after tempering. Two types of boundaries are identified: prior austenite grain boundaries and lath boundaries. Right corner: line scan of a $M_{23}C_6$ carbides on a PAGB.

boundaries in a replica is based on the principle that PAGB and lath or block boundaries are preferential sites for nucleation of precipitates. In fact, nucleation of most $M_{23}C_6$ carbides is produced on PAGB and lath or block boundaries, this allows the boundaries replication during the extraction process. Moreover, Fig. 2 shows a line scan of $M_{23}C_6$ carbides that formed at PAGB, the main observed elements of this particle were Cr, Fe, W and V. Additionally, $M_{23}C_6$ carbides were the most abundant precipitates in the microstructure, which is in agreement with the thermodynamic calculation of volume fraction of the precipitates at 780 °C (Table 2).

Fig. 3 presents a STEM dark field mode image, showing $M_{23}C_6$ carbides. The EDS analysis of an individual particle identified Cr, Fe and W as main elements; similar to the line scan results shown in Fig. 2. This is in agreement with the chemical composition calculated with Thermo-Calc at 780 °C (initial state).

Nano-sized MX particles (Nb-rich and V-rich particles) were identified by STEM. The TEM-EDS measurement showed that the main elements in the Nb-MX particles (spheroidal shape) were Nb, V and Cr (Fig. 4A). On the other hand, V-MX particles presented a rounded and plate-like shape (Fig. 4B) [29,38]. The EDS spectrum of

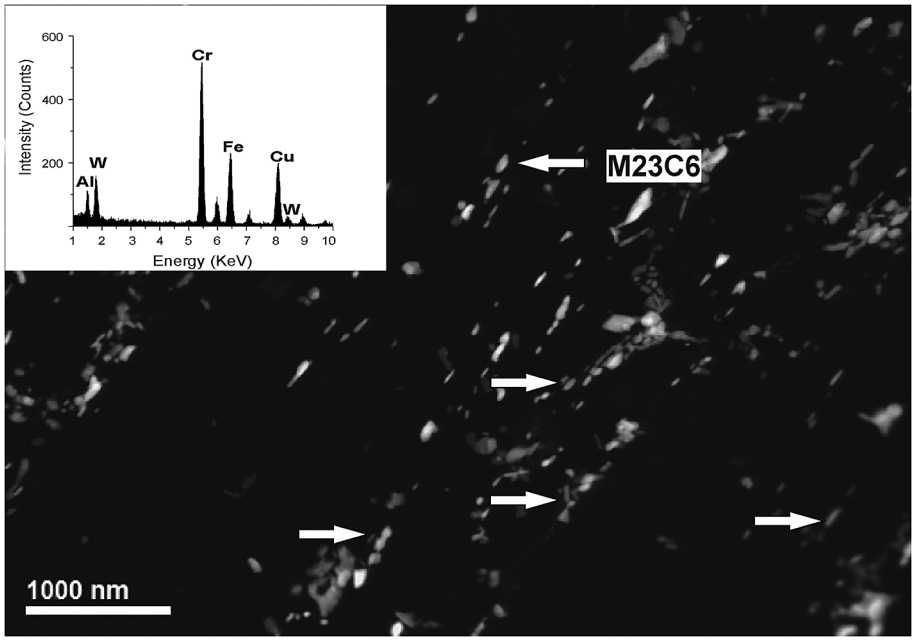

Fig. 3. STEM image, carbon extracted replica of the alloy 10.5CrWVNb at initial state (dark field) and corresponding EDS spectrum of $M_{23}C_6$ precipitates (white arrows). The Al and Cu peaks correspond to the TEM grid that holds the extracted replica.

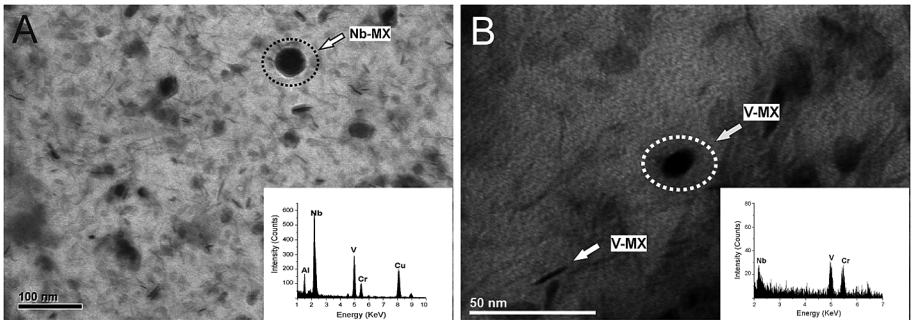

Fig. 4. STEM images, carbon extracted replication of alloy 10.5CrWVNb (bright field) at initial state, showing Nb-MX particles and EDS spectrum of the encircled particle A) and V-MX particles and EDS spectrum of the encircled V-MX particle.

the encircled V-MX carbides (Fig. 4B) showed that the main elements of V-MX particles were V, Cr and Nb. The presence of Cr in the V-rich could be explained by contamination of the film with residual Cr from the matrix in the replication extraction process. This may cause an overestimation of the content of Cr in the analyzed particles. To ensure a good identification of V-MX carbonitrides High Resolution Transmission Electron Microscopy (HR-TEM) was used. Fig. 5 shows a high resolution image of a V-MX particle and its diffraction pattern obtained by Fast Fourier Transformation analysis. The particle can be indexed as FCC with a lattice parameter a = 0.413 nm. The obtained results confirmed the precipitation of V-MX during annealing at 780°C/2 h (instead of the predicted thermodynamic stable Z phase).

The observed particles are in agreement with the predicted phases calculated by Thermo-Calc, except for Z-phase. Z-phase is a thermodynamically stable phase at 780 °C according to the Thermo-Calc calculation. However, the precipitation of this phase is expected under service conditions after several thousand hours, due to its slow kinetic of precipitation [30]. The particle sizes of the precipitates after tempering at 780 °C are shown in Table 3. The measurements are similar to those reported in previous studies of 9% Cr steels, also with similar composition [10].

3.3.2. *Microstructure after isothermal aging at 650 °C, 1440 h*

Fig. 6 shows a STEM image (carbon extracted replica) after isothermal aging by 1440 h at 650 °C. It was found that the most abundant precipitates in the microstructure were $M_{23}C_6$ carbides and Laves phase. $M_{23}C_6$ carbides showed high stability without substantial changes in particle size indicating a low coarsening rate (79 nm initial state to 80 nm after 1440 h). It has been reported that the addition of B stabilizes $M_{23}C_6$ carbides due to the enrichment of B within the particles, reducing the Ostwald ripening rate of $M_{23}C_6$ carbides [34,35]. Laves phase particles were observed after 1440 h of isothermal aging at 650 °C (Fig. 7). The EDS spectrum showed that the main elements detected in Laves phase were W, Fe, Cr and Si with a sublattice structure type $(Fe, Cr, Si)_2W$. Furthermore, Fig. 7 shows that Laves phase tends to form on PAGB near $M_{23}C_6$ carbides as clusters. Isik et al. [39] studied the nucleation of the Laves phase during high temperature exposure. It was found that before the nucleation of Laves phase, Si and Mo segregate to the micrograin boundaries, then Laves phase formed next to $M_{23}C_6$ carbides. In the alloy 10.5CrWVNb (present study), the element that promotes the formation of Laves phase is W (no Mo was added) therefore, the segregation of W along the PAGB is expected. The measured particle size of Laves phase after 1440 h at 650 °C was 227 nm (see Table 3), which can be considered as fast growth kinetics. Table 4 shows the alloy average hardness at initial state (tempering 780/2 h) and after aging at 650 °C. The hardness after 1440 h at 650 °C showed higher values in comparison to the hardness values measured at the initial state (tempering 780°/2 h). This can be explained by the precipitation of Laves phase during 1440 h. The dispersion obtained at this state of aging showed an inter-particle spacing that promoted enough precipitation hardening to compensate the reduction of solid solution hardening due to depletion of W from the matrix [6,33].

3.3.3. *Microstructure after isothermal aging at 650 °C, 8760 h*

The $M_{23}C_6$ carbides showed a slight increment in the mean

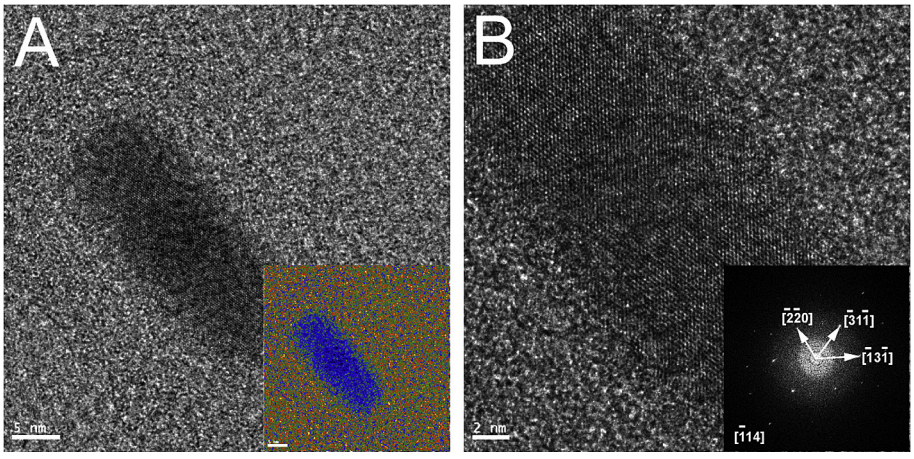

Fig. 5. HRTEM image, carbon extracted replication of alloy 10.5CrWVNb (bright field) initial state showing: A) V-MX particle, B) FFT analysis of V-MX particle.

Table 3
Mean average particle size (time in hours and size in nanometers), error = $d \pm k_1 \times S$, where S is the standard deviation and $k_1 = 1.96/\sqrt{n}$ and n is the number of measured precipitates.

Phase	0 h	1440 h	8760 h
$M_{23}C_6$	79 ± 7	80 ± 5	92 ± 3
Nb-MX	31 ± 1	32 ± 2	32 ± 1
V-MX	29 ± 1	30 ± 1	31 ± 2
Laves Phase	–	227 ± 19	303 ± 19
Z-Phase	–	–	–

Table 4
Hardness of the alloy 10.5CrWVNb for initial state, 1440 h and 8760 h.

Aging time (h)	HV10
0	270 ± 6
1440	288 ± 5
8760	260 ± 7

particle size from 79 at the initial state to 92 nm due to the coarsening of the particles (Fig. 8). On the other hand, Laves phase particles grew from 227 (1440 h) nm to 302 nm after 8760 h of isothermal aging at 650 °C (Fig. 9). As reference, in a previous study regarding the kinetic of Laves phase in a similar 9%Cr alloy [40], the average particle size of Laves phase after 8000 h under creep conditions (650°C/100 MPa) was 379 nm, in both cases Laves phase presented a fast growth kinetic. The quantification of Nb-MX and V-MX carbonitrides showed a slow coarsening rate. About 100 MX particles were measured, where Nb-MX presented an average particle size of 32 nm and V-MX presented an average particle size of 31 nm (see Table 3).

The alloy hardness after 8760 h at 650 °C decreased in comparison to the initial state, and after 1440 h of isothermal aging at 650 °C (Table 4). The explanation for this behavior may be related to the growth of the inter-particle distance of Laves phase and the growth of the particles. This phenomenon reduced the pinning effect of Laves phase particles on the dislocations and internal interfaces boundaries. Therefore, Laves phase may not longer compensate the lost of solid solution hardening due to depletion of W in the matrix by precipitation hardening [41].

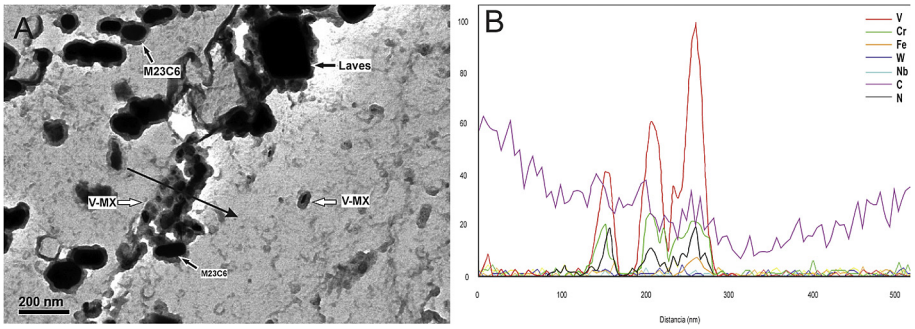

Fig. 6. STEM image of the 10.5CrWVNb after aging during 1440 h at 650 °C (bright field) (A) showing $M_{23}C_6$ carbides, Laves phase and V-MX particles. (B) Line scan of black arrow zone in A.

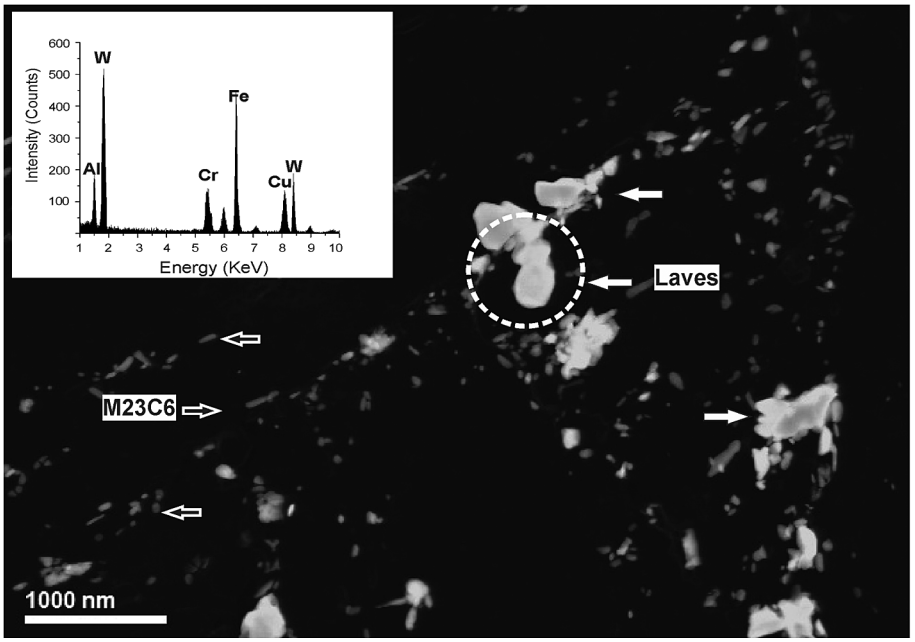

Fig. 7. STEM image of the alloy 10.5CrWVNb after aging during 1440 h at 650 °C (dark field) showing $M_{23}C_6$ carbides (black arrows) and Laves phase (white arrows). EDS spectrum of the encircled Laves phase.

3.4. Kinetic simulations (PRISMA and DICTRA)

3.4.1. Simulation of nucleation, growth and coarsening of $M_{23}C_6$ carbides calculated by PRISMA

The kinetic of precipitation during tempering at 780°C/2 h and after isothermal aging at 650 °C of $M_{23}C_6$ carbides was simulated by TC-PRISMA. Experimental data was used to fix the boundary conditions in the simulation. The grain boundary size input was set at 40 μm, the simulation time was 2 h at 780 °C for the tempering treatment and 10000 h at 650 °C considering isothermal aging. The elements Fe, C, Cr, W and Co were included for the simulation because they represent the key elements to the diffusion kinetics in the studied system [14]. Although the new database MobFe2 includes B, this element was not considered due to problems during the simulation (The B effect in TC-PRISMA software is not yet well defined). However, in order to simulate the B effect in the kinetic of particles formation, atomic mobility along grain boundary was reduced. To perform the simulation, heterogeneous nucleation on the grain boundaries was assumed; this assumption is validated by the literature and by the experimental STEM results [14]. Fig. 10 shows the results of the simulation regarding nucleation, growth and coarsening of $M_{23}C_6$ carbides. The simulation of the precipitation behavior was carried out with an interfacial energy of 0.3 and 0.1 J/m^2 (mobility of database MobFe2); in both cases, poor agreement with the experimental results was obtained. The best results were obtained reducing the atomic mobility along grain boundary and setting the interfacial energy at 0.3 J/m^2 (see Table 5). In this study, the calculated mean radius showed an excellent correlation to the experimental measurements obtained by the STEM analysis, as it is shown in Fig. 10. This is in agreement with the reported effect of B, which has been used to decrease the coarsening rate of $M_{23}C_6$ carbides [12,34]. The coarsening process can be described by the interface velocity, which depends on the interfacial energy, the mobility, the chemical composition at the interface, the driving force, and the particle radius [14,18,22]. Therefore, a reduction in the mobility and/or a reduction in the interfacial energy tends to reduce the interface velocity and the coarsening rate. Indeed, Hald et al. [42] postulate that the coarsening rate reduction related to B additions to 9%Cr heat resistant steel may influence the interfacial energy and/or the diffusivities. In the case of TC-PRISMA, when the interfacial energy is reduced from 0.3 to 0.1 J/m^2, the mean radius obtained by $M_{23}C_6$ after tempering at 780 °C was smaller than the experimental results. In contrast, the coarsening rate of $M_{23}C_6$ at 650 °C obtained by the simulation was much larger than the experimental results. This behavior may be explained considering that it is not enough to reduce the interfacial energy to accurately simulate the B effect on the precipitation kinetic of $M_{23}C_6$ carbides, also a reduction of the grain boundary mobility is required. It is important to note that it is not possible to modify the diffusivities of the elements by the users on TC-PRISMA software, nevertheless it is possible to modify the activation energy for the grain boundary diffusion. If positive activation energy is considered, the mobility of the grain boundary tends to decrease, a similar effect is expected if the diffusion coefficient of the elements is reduced. The process of stabilization of $M_{23}C_6$ carbides has been studied by F. Abe, he proposed that B segregate at grain boundaries during the austenitization process (1080/0.5 h), subsequently during the tempering, (780/2 h) $M_{23}C_6$ carbides nucleate and grow, including B in the atomic structure, which promotes the reduction the Oswald ripening rate of $M_{23}C_6$ [43].

3.4.2. Simulation of coarsening of $M_{23}C_6$ carbides calculated by DICTRA

The coarsening simulation of $M_{23}C_6$ carbides was performed by DICTRA employing the Coarsening Mode. Experimental data were also used to fix the boundary conditions in the simulation. The initial particle diameter considered for the simulation was 79 nm (obtained experimentally) and a cell size of 0.17 μm was set. The elements Fe, C, Cr, W and Co were included in the calculations performed by DICTRA because they are directly involved in the kinetics of the phase transformation. Due to the limitation of the database, B was not added to the simulation. Fig. 11 shows the behavior of the mean particle size of $M_{23}C_6$ with time and the experimental results measured by STEM (pointed out in the figure). Due to the possibility of changing the interfacial energy in the DICTRA program, different calculations were carried out with values between 0.1 and 0.9 J/m^2. The best correlation between experimental data and DICTRA calculations was found for an

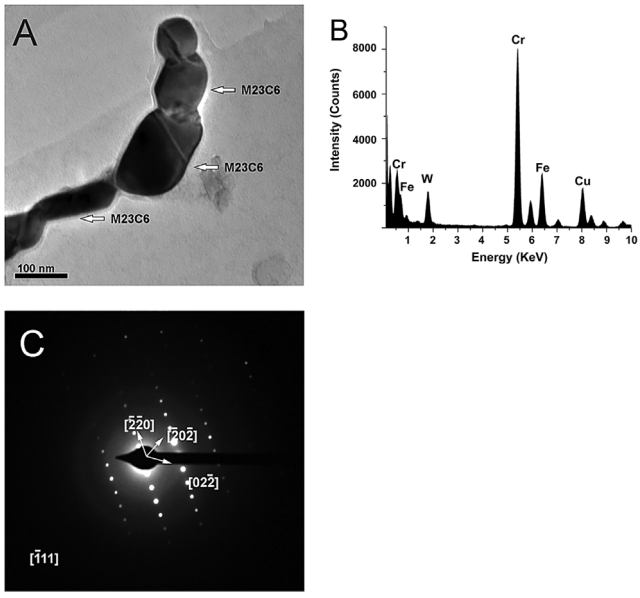

Fig. 8. STEM image, carbon extracted replication of the alloy 10.5CrWVNb after aging during 8760 h at 650 °C (dark field) showing: (A) $M_{23}C_6$ carbides, (B) EDS spectrum and (C) Diffraction Pattern.

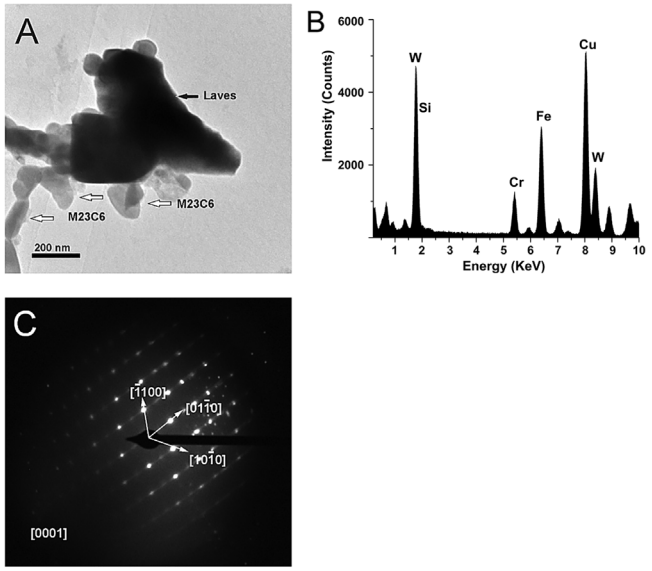

Fig. 9. STEM image, carbon extracted replication of the alloy 10.5CrWVNb after aging during 8440 h at 650 °C (dark field) showing: (A) Laves Phase (black arrows), (B) EDS spectrum and (C) Diffraction Pattern.

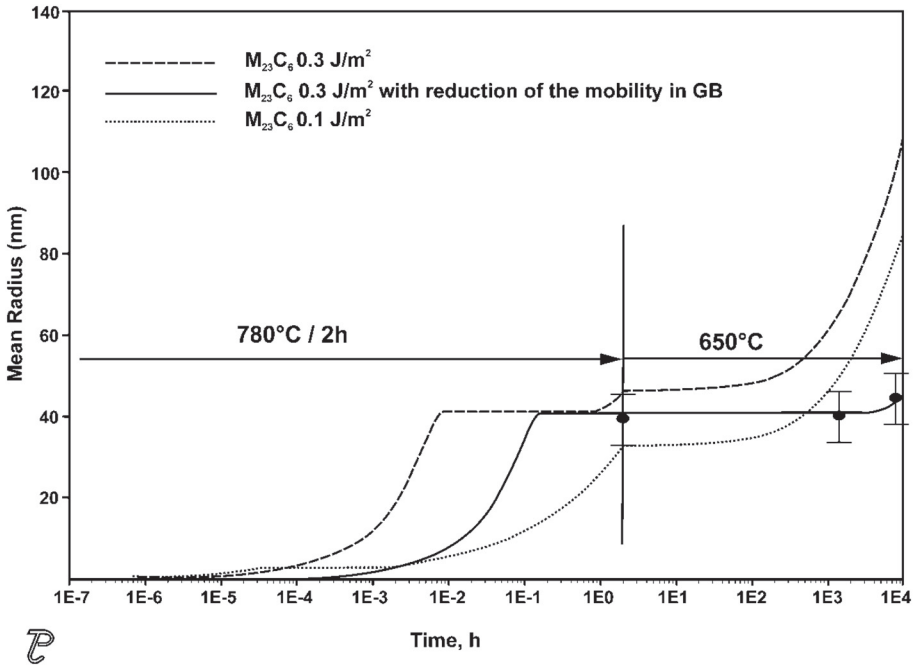

Fig. 10. Simulation of $M_{23}C_6$ carbides precipitation kinetic calculated by TC-PRISMA for the alloy 10.5CrWVNb. The points represent the experimental data.

Table 5
Physical parameters used for the $M_{23}C_6$ carbide simulation, carried out by TC-PRISMA.

Interfacial Energy (J/m²)	Grain Boundary Size (μm)	Phase energy addition ΔG (J/mol)	Mobility Enhancement Factor Q_{GB} (J/mol)	Interfacial Mobility ν (m⁴/Js)
0.3	40	Default TCFe7	Default MobFe2	Default MobFe2
0.1	40	Default TCFe7	Default MobFe2	Default MobFe2
0.3	40	Default TCFe7	30000	Default MobFe2

interfacial energy of 0.1 J/m^2. In general, it is expected that $M_{23}C_6$ carbides nucleate with interfacial energy between 0.1 and 0.5 J/m^2 due to its semi-coherent interface with the matrix. In previous works Prat et al. calculated the precipitation of these particles in 9% Cr with B content. It was found that the best correlation between the experimental data and interfacial energy was at 0.1 J/m^2 [14]. In previous investigations [44], coarsening calculation of $M_{23}C_6$ were performed by DICTRA in a 12%Cr steels with B content, showing that the best agreement with the experimental results was obtained with an interfacial energy of 0.1 J/m^2. Furthermore, Xiang Xiao et al. studied the coarsening of $M_{23}C_6$ carbides in a 12%Cr steel with no B addition, finding that the best agreement between the simulation and the experimental data was obtained with an interfacial energy of 0.5 J/m^2 [45]. This suggests that B reduces the lattice misfit between the matrix and $M_{23}C_6$ carbides, changing the conditions at the interface and affecting the diffusivities [43,44]. Therefore, B additions effectively reduced the coarsening rate of $M_{23}C_6$ carbides.

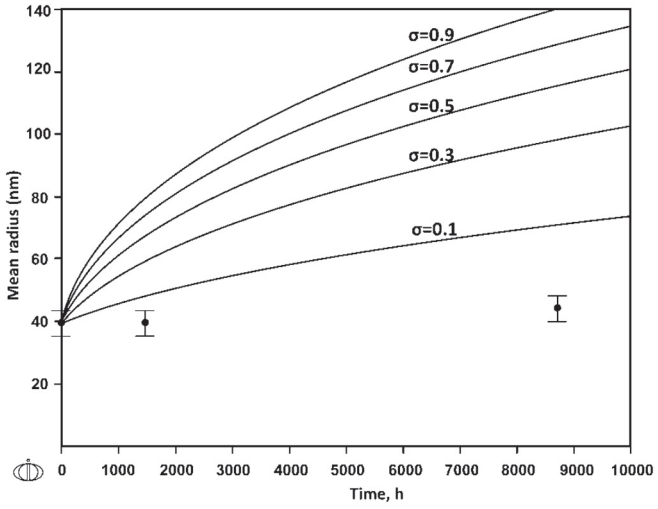

Fig. 11. Simulation of coarsening of $M_{23}C_6$ carbides with different interfacial energies calculated by DICTRA for the alloy 10.5CrWVNb at 650 °C. The points represent the experimental data.

Fig. 12 shows the curves obtained by TC-PRISMA calculations with different border condition (different interfacial energy and mobility on the GB) and DICTRA calculation. The best result was obtained by the TC-PRISMA calculation with an interfacial energy of 0.3 J/m^2 and a reduced atomic mobility along grain boundary. These parameters allow to consider the effect of B in the TC-PRISMA calculations, which decrees the coarsening rate of $M_{23}C_6$. This is in correlation to the fact that $M_{23}C_6$ carbides nucleate heterogeneously in lath and grain boundaries. This suggests that the nucleation process of $M_{23}C_6$ carbides occurs with a semi-coherent interface. Therefore, an interfacial energy of 0.3 J/m^2 for the precipitation process is in agreement with the literature, the simulation by PRISMA and the experimental results. The DICTRA simulation showed the best correlation with an interfacial energy of 0.1 J/m^2. It is important to note that the simulation performed by DICTRA did not include the effect of B addition. As was mentioned

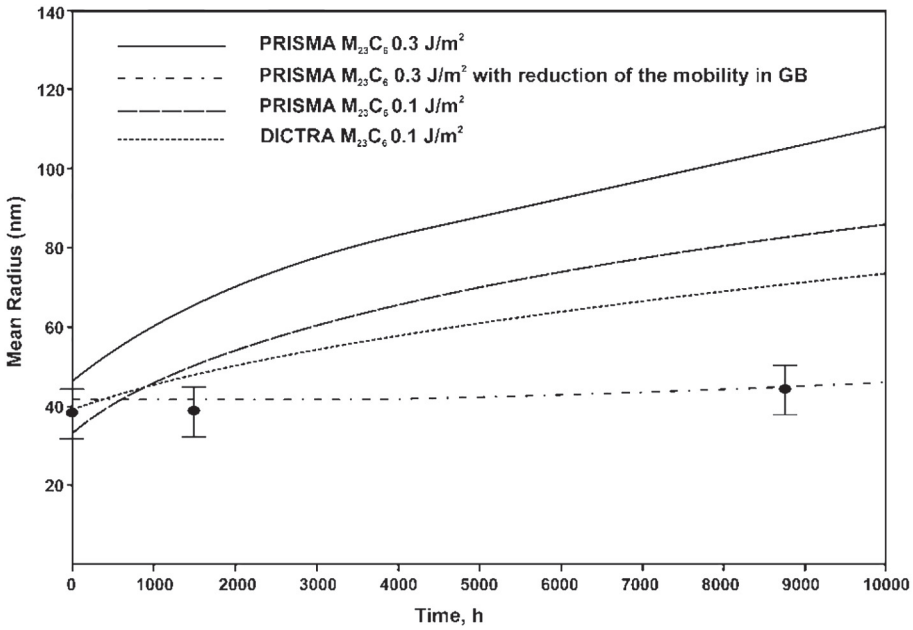

Fig. 12. Coarsening stages comparison of TC-PRISMA and DICTRA calculations carried out to the $M_{23}C_6$ carbides.

above, B reduces the coarsening rate of $M_{23}C_6$ carbides by the reduction of the interfacial energy and the diffusion coefficient of its constitutive elements. After about 9000 h the DICTRA simulations obtained larger mean radius values than the experimental result, due to the effect of B content, which reduces the coarsening rate of $M_{23}C_6$ carbides [9].

3.4.3. Simulation of nucleation, growth and coarsening of Laves Phase calculated by TC-PRISMA

The nucleation, growth and coarsening simulation of Laves phase at 650 °C was carried out by TC-PRISMA. The elements considered to perform the calculations were Fe, C, Cr, Co, W and Si, which have direct influence on the kinetic precipitation of Laves phase. Due to the incoherent nature of the Laves phase, an interfacial energy of 0.6 J/m^2 was selected [42,46,47]. Phase energy addition and grain boundary diffusion were assumed. Fig. 13 shows good correlation between the TC-PRISMA calculations of Laves phase precipitation and the experimental values obtained by STEM. The precipitation behavior of Laves phase in 9–12%Cr heat resistant steel has been simulated by several authors using MatCalc and DICTRA. However, according to the best of our knowledge, there are not publications available in which TC-PRISMA calculations are compared to experimental long-term results. The nucleation and growth process of Laves phase is mainly controlled by W, Mo and Si, atoms, which present slow diffusivity in the martensitic/ferritic matrix [3,8,9]. Therefore, long experimental campaigns are needed in order to validate the kinetics simulation. Isik et al. [39] studied the nucleation of Laves phase in an 11.7%Cr alloy. They found that prior to the nucleation, Si and Mo segregate in micro-grain boundaries. Hence, Laves phase can nucleate after several hundred hours at 650 °C, once that thermodynamic and kinetic conditions at the grain boundary are changed; the driving force (equation (4)) and the atomic mobility along grain boundaries must surpass the thermodynamic barriers to nucleate and grow. A similar behavior is expected in the alloy 10.5CrVNb, where W was added instead of Mo. In agreement with the previous explanation, the "Phase Energy Addition" parameter was modified in order to change the thermodynamic conditions. Moreover, the "Grain Boundary Diffusion" parameter was modified to change the kinetic conditions on the grain boundary. It is very important to note that the nucleation and growth of the Laves phase will only start when these two parameters reach certain value, which allows to surpass the activation energy for the precipitation. Table 6 summarizes the values used for the calculation of Laves phase precipitation. It is important to note that to accurately simulate the relationship between the Laves phase and the ferritic matrix, a small interface mobility value must be used. With this small value, it is possible to consider an immobile interface at initial stage. However, after about a hundred hours, the interface mobility rapidly increases to higher values, leading to the quick growth of the mean radius, as can be observed in Fig. 13. These three conditions may be considered to effectively simulate the micro-segregation of W and Si in PRISMA. It has been observed that the boundary condition for simulation of the nucleation process of Laves phase in PRISMA depends on the chemical composition of the alloy. After the nucleation, the growth

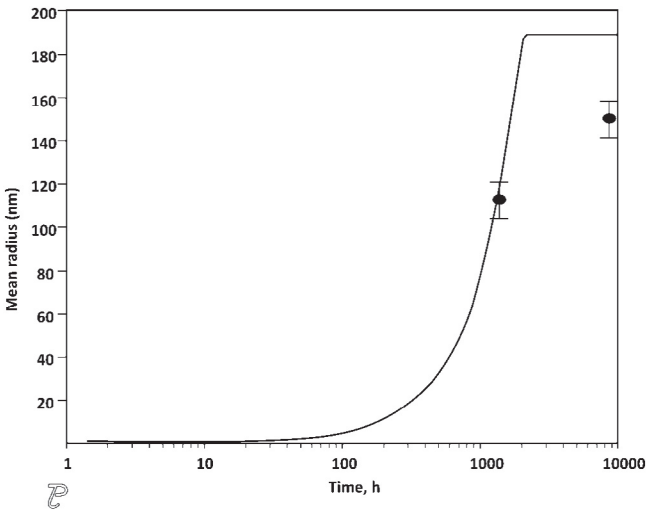

Fig. 13. Simulation of the Laves Phase precipitation kinetic calculated by TC-PRISMA for the alloy 10.5CrWVNb. The points represent the experimental data.

Table 6
Physical parameters used by TC-PRISMA for the simulation of Laves phase.

Interfacial Energy (J/m^2)	Grain Boundary Size (μm)	Phase energy addition ΔG (J/mol)	Mobility Enhancement Factor Q_{GB} (J/mol)	Interfacial Mobility ν (m^4/Js)
0.6	40	−10000	−90000	1.00×10^{-23}

process begins approximately at 20 h of isothermal aging at 650 °C reaching a particle size of 234 nm (227 ± 19 nm experimental) at 1440 h and 380 nm at 8760 h (303 ± 19 nm experimental). An explanation for the observed difference between the TC-PRISMA calculation and the experimental values at 8760 h/650 °C isothermal aging may be related to the effect of the interfacial energy in the growth rate of Laves phase. For smaller interfacial energy values, a better fit between the simulated and experimental results is expected. However, smaller interfacial energy values (<0.6 J/m^2) describe a semi-coherent interface, which is not corroborated by the experimental observations [15,39]. For the nucleation and growth process of Laves phase, two mechanisms have been described in the literature [43]. The first is the nucleation and growth of Laves phase in the martensite lath and/or subgrain boundaries without the presence of $M_{23}C_6$ carbide in the vicinity of the Laves phase particles. For this case the Laves phase particles are coherent with one side of the grain boundary and incoherent with the other side, the Laves phase grow into grain with the incoherent interface, due to incoherent interface have higher mobility [40,48]. The second one is the nucleation and growth of Laves phase at Cr-depleted zones adjacent to $M_{23}C_6$ carbides [40,49]. The predominant mechanism that controls the precipitation process depends on the chemical composition of the alloy. It is expected that in the alloy 10.5CrWVNb, the predominant mechanism is the second one [40], in this case TC-PRISMA may not consider the effect of $M_{23}C_6$ carbides in the precipitation behavior of Laves phase.

Table 7
Thermodynamics parameters calculated (Thermo-Calc) for the Laves phase nucleation at 650 °C. Interfacial energy assumed is 0.6 J/m^2.

Phase	Driving force ΔG*(J/mol)	Molar Volume V_m(m^3)	Critical radius r*(m)
Laves	1407	7.96×10^{-6}	6.78×10^{-9}

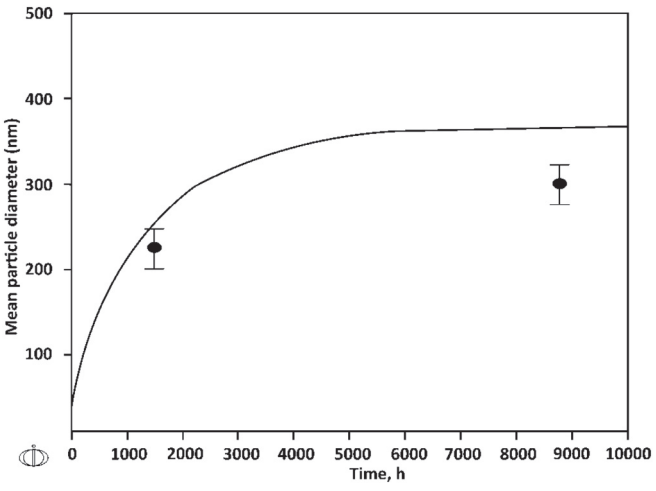

Fig. 14. Simulation of the Laves phase growth kinetic calculated by DICTRA for the alloy 10.5CrWVNb at 650 °C. The points represent the experimental data.

3.4.4. Simulation of growth of Laves Phase calculated by DICTRA

The growth of Laves phase was simulated by DICTRA. The only elements having an influence in the Laves phase growth kinetics were (Fe, C, Cr, Co, W, Si) [9]. For the critical radius calculation, thermodynamic parameters, such as the nucleation driving force and the molar volume, were calculated by Thermo-Calc (see Table 7). A critical radius of 6.78 nm was determined considering an incoherent interface between the Laves phase with the surrounding matrix, and an interfacial energy of 0.6 J/m^2 [9,15,40]. Cell size was experimentally calculated obtaining 0.8 μm. The Laves phase mean particle diameter calculated by DICTRA showed good agreement with the experimental results (Fig. 14). On the other hand, the simulation showed that the growth process of Laves phase began approximately after 20 h at 650 °C and reached a particle size of 250 nm (227 ± 19 nm experimental) at 1440 h and 365 nm (303 ± 19 nm experimental) at 8760 h. Good agreement between the experimental results, TC-PRISMA and DICTRA calculations were observed. However, the TC-PRISMA calculation introduced the possibility of simulating all the precipitation stages (nucleation, growth and coarsening). Hence, the effect of chemical composition in particle size distribution, number density, volume fraction and nucleation rate can be simulated [9,15].

4. Conclusions

In the present study a 10.5%Cr heat resistant steel was designed and produced assisted by Thermo-Calc. The studied alloy was characterized at the initial state (tempering at 780°C/2 h), and after 1440 h and 8760 h under isothermal aging at 650 °C (2 moths and 1 year respectively at 650 °C). The obtained experimental results were compared to the kinetic calculations carried out by TC-PRISMA and DICTRA software. In general, a good agreement between the TC-PRISMA and DICTRA software was found with the experimental results. The conclusions of this study are summarized as follows:

- The TEM characterization at the initial state (tempering 780°C/2 h) showed the precipitation of $M_{23}C_6$ carbides, Nb-MX and V-MX carbonitrides with an average particle size of 79, 30 and 29 nm, respectively. No Laves and Z phase were found at this initial state.
- The TEM characterization of a sample aged for 1440 h (2 months) at 650 °C showed high stability of $M_{23}C_6$ carbides and MX carbonitrides, no substantial variation of particle size was found due to the slow coarsening rate of these particles. Laves phase particles were observed at this state of aging with an average particle size of 220 nm.
- The TEM characterization of the precipitates after 8760 h at 650 °C of isothermal aging showed very slow coarsening rate of the Nb-MX and the V-MX carbonitride almost without variation in particle size. The $M_{23}C_6$ carbide showed good stability with an increment of 10% in particle size. On the other hand, Laves Phase showed a poor stability reaching 303 nm after 8760 h at 650 °C. No Z phase was found.
- The $M_{23}C_6$ carbide calculations performed by TC-PRISMA considering an interfacial energy of 0.3 J/m^2 and a "reduction of the mobility in grain boundary" showed excellent agreement

with the experimental results. These conditions effectively simulated the B effect on the $M_{23}C_6$ coarsening rate.

- The $M_{23}C_6$ carbide calculations performed by DICTRA showed good agreement with the experimental results with an interfacial energy of 0.1 J/m^2. Nevertheless, the interfacial energy obtained by the simulation does not agree with a semi-coherent precipitate. This may be related to the B effect on the $M_{23}C_6$ coarsening rate, which it is not considered in the calculations.
- The simulation of nucleation, growth and coarsening of Laves phase was carried out by TC-PRISMA. Good results were obtained between the calculations and the experimental data. An interfacial energy of 0.6 J/m^2 was used, and the "phase energy addition" parameter and the "grain boundary diffusion" term were activated to reproduce the segregation of W and Si in grain boundary. Once these conditions are activated, the precipitation process of the Laves phase may start for the alloy 10.5CrWVNb.
- The Laves phase growth simulations were carried out by DICTRA, good agreement with the experimental results were found for an incoherent interface energy of 0.6 J/m^2.

Acknowledgments

The authors would like to thank in particular: "DOCTORADO NACIONAL 21130630" for Doctoral Research Fellowship. Also, project "FONDECYT de Iniciación 11110098″, Project "FONDECYT de Iniciación 11121384″, "Proyecto de inserción de capital humano avanzado 79112035″ and project "FONDECYT 1150457" from the Chilean Government, for the financial support of this work. The authors are grateful for the support of the Create-Net project (H2020-MSCA-RISE/644013) for research stays.

References

[1] M. Staubli, K.-H. Mayer, T.-U. Kern, R.W. Vanstone, R. Hanus, J. Stief, K.-H. Schönfeld, in: R. Viswanathan, W.T. Bakker, J.D. Parker (Eds.), Proc. COST 522-Power Generation into the 21st Century; Advanced Steam Power Plant, University of Wales and EPRI, 2001, pp. 15–32.
[2] N. Tanaka, R. Wicks, Power Generation from Coal. Measuring and Reporting Efficiency Performance and CO2 Emissions, International Energy Agency, Paris, Francia, 2010.
[3] J. Hald, Int. J. Pres. Ves.Pip. 85 (2008) 30–37.
[4] H. Mayer, F. Masuyama, The development of creep-resistant steels, in: F. Abe, T.-U. Kern, R. Viswanathan (Eds.), Creep Resistant Steels, Woodhead Publishing in Materials, Cambridge, 2008, pp. 15–77.
[5] D. Rojas, J. Garcia, O. Prat, C. Carrasco, G. Sauthoff, A.R. Kaysser-Pyzalla, Mater. Sci. Eng. A 527 (2010) 3864–3876.
[6] J. Pešička, R. Kužul, A. Dronhofer, G. Eggeler, Acta. Mater. 51 (2003) 4847–4862.
[7] P.J. Ennis, A. Zielinska-Lipiec, O. Wachter, A. Czyrska-Filemonowicz, Acta Mater. 45 (1997) 4901–4907.
[8] A. Aghajani, C. Somsen, G. Eggeler, Acta Mater. 57 (17) (2009) 5093–5106.
[9] O. Prat, J. Garcia, D. Rojas, C. Carrasco, G. Inden, Acta Mater. 58 (2010) 6142–6153.
[10] D. Rojas, J. Garcia, O. Prat, G. Sauthoff, A.R. Kaysser-Pyzalla, Mater. Sci. Eng. 528 (2011) 5164–5176.
[11] S. Straub, M. Meier, J. Ostermann, W. Blum, VGB Kraftw. 73 (1993) 646–653.
[12] F. Abe, Mater. Sci. Eng. A 510–511 (2009) 64–69.
[13] A. Kostka, K.-G. Tak, R.J. Hellmig, Y. Estrin, G. Eggeler, Acta Mater. 55 (2007) 539–550.
[14] O. Prat, J. García, D. Rojas, J.P. Sanhueza, C. Camurri, Mater. Chem. Phys. 143 (2014) 754–764.
[15] A. Schneider, G. Inden, Acta Mater. 53 (2005) 519–531.
[16] THERMO-CALC: Thermodynamic Equilibrium Calculation.s, http://www.thermocalc.com/products-services/software/thermo-calc/
[17] TCFE7 S Version, TCC Steels and Fe-alloys Data Base provided by Thermo-calc Software AB, 2011. http://www.thermocalc.com/products-services/databases/.
[18] TC-PRISMA: Thermodynamic and Diffusion Calculations., http://www.thermocalc.com/products-services/software/tc-prisma/
[19] J. Feder, K.C. Russell, J. Lothe, G.M. Pound, Adv. Phys. 15 (1966) 111–178.
[20] J.D. Verhoeven, Fundamentals of Physical Metallurgy, Wiley, New York, 1975, pp. 389–397.
[21] J. Svoboda, F.D. Fisher, P. Fratzl, E. Kozeschnik, Mat. Sci. Eng. A 385 (2004) 166–174.
[22] DICTRA: Diffusion Controlled Reactions in Multi-component Alloy Sy.stems, http://www.thermocalc.com/products-services/software/dictra/
[23] A. Borgenstram, A. Engstrom, L. Hoglund, J. Agren, DICTRA, J. phase Equilibria 21 (3) (2000) 269–280.
[24] I.M. Lifshitz, V.V. Slyozov, J. Phys. Chem. Solids 19 (1961) 35–50.
[25] C. Wagner, Z. Electrochem. 65 (1961) 581–591.
[26] A. Engström, MOB2 Mobility Database, Thermo-calc AB, Royal Institute of Technology, Stockholm, 1998.
[27] D.R.G. Mitchell, S. Sulaiman, Mater. Charact. 56 (2006) 49–58.
[28] A. Bjärbo, M. Hättestrand, Metall. Mater. Trans. A 32 A (2001) 19–27.
[29] L. Cipolla, H.K. Danielsen, D. Venditti, P.E. Di Nunzio, J. Hald, M.A.J. Somers, Acta. Mater 58 (2010) 669–679.
[30] H.K. Danielsen, P.E. DiNunzio, J. Hald, Metall. Mater. Trans. A 44A (2013) 2445–2452.
[31] U.E. Klotz, C. Solenthaler, P. Uggowitzer, Mat.Sci. Eng.A 476 (2008) 186–194.
[32] L. Helis, Y. Toda, T. Hara, H. Miyazaki, F. Abe, Mater. Sci. Eng. A 510–511 (2009) 88–94.
[33] P. Hu, W. Yan, W. Sha, W. Wang, Z. Guo, Y. Shan, K. Yang, Front. Mater. Sci. 3 (4) (2009) 434–441.
[34] F. Abe, T. Horiuchi, M. Taneike, K. Sawada, Mater. Sci. Eng. A 378 (2004) 299–303.
[35] P. Hofer, M.K. Miller, S.S. Babu, S.A. David, H. Cerjak, Metall. Mater. Trans. A 31A (2000) 975–984.
[36] T. Onizawa, T. Wakai, M. Ando, K. Aoto, Nucl. Eng. Des. 238 (2008) 408–416.
[37] D. Rojas, J. Garcia, O. Prat, C. Carrasco, G. Sauthoff, A.R. Kaysser-Pyzalla, Mater. Sci. Eng. A 528 (2011) 1372–1381.
[38] K. Yamada, M. Igarashi, S. Muneky, F. Abe, ISIJ Int. 41 (2001) S116–S120.
[39] M.I. Isik, A. Kostka, G. Eggeler, Acta. Mater. 81 (2014) 230–240.
[40] O. Prat, J. Garcia, D. Rojas, G. Sauthoff, G. Inden, Intermetallics 32 (2013) 362–372.
[41] Jie Cui, Ick-Soo Kim, Chang-Yong Kang, Kazuya Miyahara, ISIJ Int. 41 (2001) 368–371.
[42] John Hald, Leona Korkacova, ISIJ Int. 43 (2003) 420–427.
[43] F. Abe, Procedia Eng. 10 (2011) 94–99.
[44] O. Prat, J. Garcia, D. Rojas, C. Carrasco, A.R. Kaysser-Pyzalla, Mater. Sci. Eng. A 527 (2010) 5976–5983.
[45] Xiang Xiao, Guoquan Liu, Benfu Hu, Jinsan Wang, Wenbin Ma, J. Mater. Sci. 48 (2013) 5410–5419.
[46] B.S. Srinivas Prasad, V.B. Rajkumar, K.C. Hari Kumar, Calphad 36 (2012) 1–7.
[47] Xi Zhi-xin, Wang Chuan-yang, Lei Chen, Lai Yun-ting, Zhao Yan-fen, Zhang Lu, J. Iron Steel Res. Int. 23 7 (2016) 685–691.
[48] M.I. Isik, A. Kostka, V.A. Yardley, K.G. Pradeep, M.J. Duarte, P.P. Choi, D. Raabe, G. Eggeler, Act. Mater. 90 (2015) 94–104.
[49] Huiran Cui, Feng Sun, Ke Chen, Lanting Zhang, Rongchun Wan, Aidang Shan, Jiansheng Wu, Mater. Sci. Eng. A 527 (2010) 7505–7509.